

Polarization-selective magneto-optical modulation

Banoj Kumar Nayak and Eyal Buks

Andrew and Erna Viterbi Department of Electrical Engineering, Technion, Haifa 32000 Israel

(Dated: September 30, 2022)

We study magneto-optical coupling in a ferrimagnetic sphere resonator made of Yttrium iron garnet. We find that the resonator can be operated in the telecom band as a polarization-selective optical modulator. Intermodulation gain can be employed in the nonlinear regime for amplification.

I. INTRODUCTION

Information is commonly transmitted by modulating a monochromatic carrier wave. The method of single side-band modulation (SSM) allows reducing both transmission power and bandwidth, in comparison with simpler methods such as amplitude, frequency and phase modulation [1]. In the radio frequency band SSM can be implemented using electronic circuits, however, SSM implementation in the optical band is challenging, since it requires that different out of phase modulation methods are simultaneously applied [2, 3].

Magneto-optical (MO) coupling [4–10] in ferrimagnetic sphere resonators (FSR) can be used for optical modulation of signals in the microwave band. Such a modulation has been demonstrated before [11–21] by exciting individual whispering gallery FSR optical modes using either a tapered optical fiber or a prism. Here we employed a modified experimental setup, in which light in the telecom band is transmitted through the FSR bulk. Driving the FSR near its resonance generates sidebands in the transmitted optical spectrum. We find that the FSR can be used as a polarization-selective SSM. The polarization selectivity is attributed to angular momentum conservation in photon-magnon scattering [22–27]. We demonstrate that intermodulation (IMD) gain can be exploited in the nonlinear regime for amplification.

II. EXPERIMENTAL SETUP

The experimental setup is schematically shown in Fig. 1. Optical components and fibers are red colored, whereas blue color is used to label microwave (MW) components and coaxial cables. A MW cavity made of a loop gap resonator (LGR) allows achieving a relatively large coupling between magnons and MW photons [29–32]. The LGR is fabricated from a hollow concentric aluminium tube. A sapphire (S) strip of $260\ \mu\text{m}$ thickness is inserted into the gap in order to increase its capacitance, which in turn reduces the frequency f_c of the LGR fundamental mode. An FSR made of Yttrium iron garnet (YIG) having radius of $R_s = 125\ \mu\text{m}$ is held by two ceramic ferrules (CF) inside the LGR. The two CFs, which are held by a concentric sleeve, provide transverse alignment for both input and output single mode optical fibers. Fiber longitudinal alignment is performed by maximizing optical transmission.

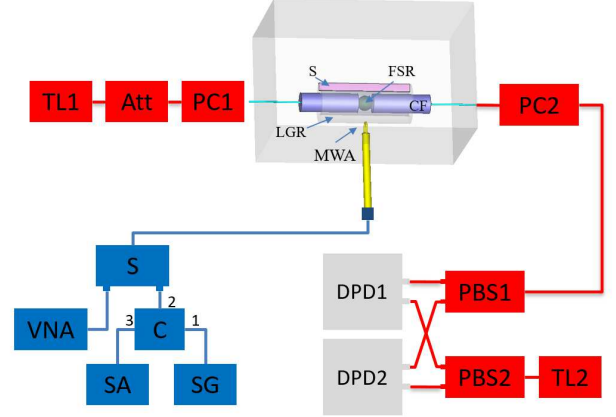


Figure 1: Experimental setup. Optical fibers are installed on both sides of the FSR for transmission of light through the sphere. Optical components [TL (tunable laser), Att (optical attenuator), PC (polarization controller) and PBS (polarization beam splitter)] and fibers are red colored, and MW components [MWA (microwave loop antenna), S (splitter), C (circulator), VNA (vector network analyzer), SA (spectrum analyzer) and SG (signal generator)] and coaxial cables are blue colored. TL2 together with two PBSs (labelled as PBS1 and PBS2) and two differential photo detectors (labelled as DPD1 and DPD2) operate as a polarization-selective optical spectrum analyzer (OSA) [28]. A power amplifier is serially connected to the SG. The MWA is weakly coupled to the FSR-LGR system.

The angular frequency of the Kittel mode ω_m is approximately given by $\omega_m = \mu_0 \gamma_e H_s$, where H_s is the static magnetic field, μ_0 is the free space permeability, and $\gamma_e/2\pi = 28\ \text{GHz T}^{-1}$ is the gyromagnetic ratio [10]. The applied static magnetic field \mathbf{H}_s is controlled by adjusting the relative position of a magnetized Neodymium using a motorized stage. The static magnetic field is normal to the light propagation direction \mathbf{k} , and the magnetic field of MW drive is nearly parallel to \mathbf{k} . The LGR-FSR coupled system is encapsulated inside a metallic rectangular shield made of aluminum. The LGR is weakly coupled to a microwave loop antenna (MWA).

The plot in Fig. 2 exhibits a vector network analyzer (VNA) reflectivity measurement of the LGR-FSR coupled system. The static applied magnetic field H_s in this measurement is varied near the value corresponding to avoided-crossing between the FSR and LGR resonances.

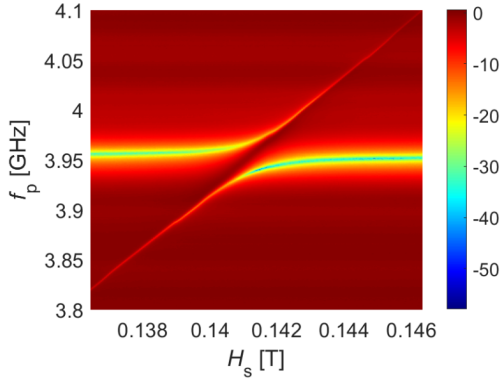


Figure 2: VNA reflectivity in dB units as a function of magnetic field H_s at applied microwave power of -30 dBm.

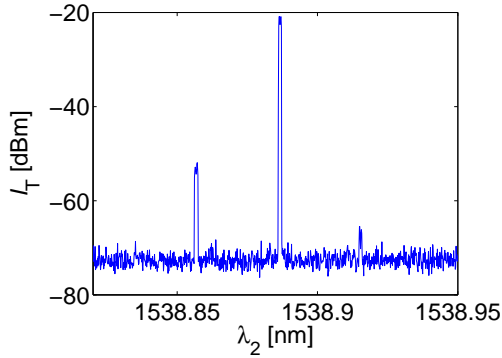


Figure 3: The transmitted optical spectrum. For this measurement the TL1 is set at optical power of 31 mW and wavelength λ_L of 1538.887 nm, and the driving microwave is set at frequency $\omega_p/(2\pi)$ of 3.79 GHz and power of P_p of 20 dBm.

III. OPTICAL SIDE BANDS

Optical side bands are observed in the transmission spectrum when the driving microwave frequency $\omega_p/(2\pi)$ is tuned close to the FSR resonance at $\omega_m/(2\pi)$. The plot shown in Fig. 3 exhibits the measured total optical intensity $I_T = I_{DPD1} + I_{DPD2}$ as a function of the wavelength λ_2 of TL2, where I_{DPD1} and I_{DPD2} are the intensities measured by the two differential photodetectors (labelled as DPD1 and DPD2 in Fig. 1). The side band wavelengths are given by $\lambda_L \pm \lambda_{SB}$, where $\lambda_{SB} \simeq \lambda_L^2 \omega_p/(2\pi c)$, and λ_L is the TL1 wavelength, which is related to the TL1 frequency $\omega_L/(2\pi)$ by $\omega_L = 2\pi c/\lambda_L$, where c is the speed of light in vacuum. The value of $\lambda_{SB} = 30.0$ pm is obtained for TL1 wavelength of $\lambda_L = 1539$ nm and FSR driving frequency of $\omega_p/(2\pi) = 3.79$ GHz.

Both motorized polarization controllers (labelled as PC1 and PC2 in Fig. 1) have three optomechanical components (paddles), which act as either quarter or half wave plates. The paddles' angles of PC1 (PC2) are denoted by θ_{1A} , θ_{1B} and θ_{1C} (θ_{2A} , θ_{2B} and θ_{2C}). The in-

cident light state of polarization (SOP) can be manipulated using PC1. We observe that intensity of lower wavelength $\lambda_L - \lambda_{SB}$ anti-Stokes sideband and higher wavelength $\lambda_L + \lambda_{SB}$ Stokes side band depend on the input SOP. SSM in the transmission spectrum, with either single anti-Stokes side band, or with single Stokes side band, can be obtained by adjusting PC1. The plot shown in Fig. 4(a) exhibits the measured anti-Stokes side band intensity as a function of microwave driving frequency $f_p = \omega_p/(2\pi)$ and PC1 angle θ_{1C} near the avoided-crossing region. The plot shown in Fig. 4(c) exhibits simultaneously measured Stokes side band intensity in the same region. We clearly observe appreciable anti-Stokes and Stokes intensity in Fig. 4 (a) and (c), respectively, when driving frequency $\omega_p/(2\pi)$ becomes close to FSR resonance $\omega_m/(2\pi)$. However, they are asymmetric. For a certain range of PC1 position, SSM is obtained, i.e. only one side band, either anti-Stokes or Stokes, is observed. Contrary to other experimental setups, in which the FSR is optically coupled by either a tapered optical fiber or a prism, for our setup, for which the measured optical transmission only weakly depends on the input wavelength λ_L , SSM can be obtained in wide range of λ_L .

A rotating lambda plate polarimeter is employed to measure the input SOP. The polarimeter measurements reveal that the input SOP for the two extreme cases (SSM of either anti-Stokes or Stokes peak) are orthogonal to each other (i.e. separated by a diameter on the Poincaré sphere).

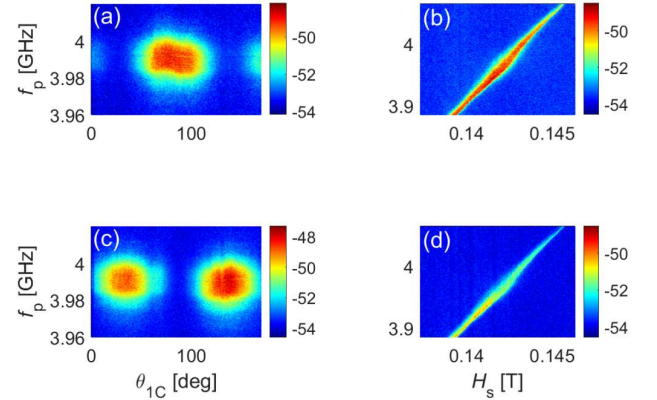


Figure 4: Side bands in dBm units. (a) anti-Stokes intensity as a function of PC1 angle θ_{1C} . (b) anti-Stokes intensity as a function of magnetic field H_s . (c) Stokes intensity as a function of θ_{1C} . (d) Stokes intensity as a function of H_s . The magnetic field H_s in (a) and (c) is tuned near avoided-crossing regime. TL1 is set at optical power of 31 mW and wavelength of λ_L of 1537.7 nm, and the driving microwave power is set at $P_p = 20$ dBm. In (a) and (c), $\theta_{1A} = 170^\circ$ and $\theta_{1B} = 85^\circ$, and θ_{1C} is varied from 0° to 170° , whereas in (b) and (d) $(\theta_{1A}, \theta_{1B}, \theta_{1C}) = (170^\circ, 85^\circ, 60^\circ)$ (for this setting both Stokes and anti-Stokes peaks are clearly visible near the FSR resonance).

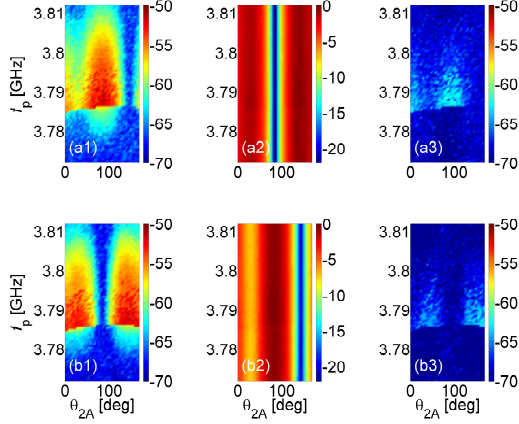


Figure 5: Sideband SOP. The measured intensity I_{DPD1} (I_{DPD2}) is shown (in dBm units) in the plots labeled by the letter 'a' ('b'). The intensity at wavelengths $\lambda_L - \lambda_{\text{SB}}$, λ_L and $\lambda_L + \lambda_{\text{SB}}$ is shown in the plots labelled by the numbers '1', '2' and '3', respectively. The TL1 is set at optical power of 31 mW and wavelength of λ_L of 1538.9 nm, the driving microwave is set at power P_p of 20 dBm.

The plots shown in Fig. 4 (b) and (d) exhibit anti-Stokes and Stokes intensity, respectively, as a function of microwave driving frequency f_p and static magnetic field H_s . The FSR resonance changes as we vary the static magnetic field H_s . Accordingly, from Fig. 4(b) and (d), we see that both anti-Stokes and Stokes intensity gets pronounced when driving frequency $\omega_p/(2\pi)$ is within the bandwidth of FSR resonance at $\omega_m/(2\pi)$.

Our experimental setup (see Fig. 1) allows measuring the SOP of both sidebands. While the plots shown in Fig. 4 display the total optical intensity $I_T = I_{\text{DPD1}} + I_{\text{DPD2}}$, the intensity I_{DPD1} (I_{DPD2}) is separately displayed in the top (bottom) row plots shown in Fig. 5. These two intensities I_{DPD1} and I_{DPD2} represent two orthogonal SOP, which can be set by adjusting PC2 (see Fig. 1). The left (right) column plots in Fig. 5 display the measured intensity of the left anti-Stokes (right Stokes) sideband at wavelength $\lambda_L - \lambda_{\text{SB}}$ ($\lambda_L + \lambda_{\text{SB}}$), whereas the intensity at the central wavelength λ_L is displayed by the central column plots in Fig. 5. For the measurements shown in Fig. 5, PC1 is set to a nearly SSM state. By varying the setting of PC2, we find that the central peak at wavelength λ_L is maximized (minimized) in the same region where the sidebands at wavelength $\lambda_L \pm \lambda_{\text{SB}}$ are minimized (maximized). This observation implies that in the region of SSM, the SOP of the sidebands is nearly orthogonal to the SOP of the incident light. This orthogonality can be exploited at the receiver end of a data transmission system based on our proposed MO modulation, since it allows demodulation by polarization filtering-out of the carrier at wavelength λ_L .

IV. MO COUPLING

The MO coupling giving rise to the optical sidebands originates from an interaction term in the system's Hamiltonian, which is denoted by V_{SB} . This term V_{SB} is commonly derived from the classical energy density associated with the interaction between magnetization and optical modes. For the case where only whispering gallery FSR optical modes participate in the interaction, the term V_{SB} was derived in [11–19], whereas for our experimental configuration we consider the case where light propagates through the FSR bulk.

Consider an incident I (scattered S) optical field, having right and left handed circular polarization amplitudes $E_{\text{I}+}$ and $E_{\text{I}-}$ ($E_{\text{S}+}$ and $E_{\text{S}-}$), respectively. The time-averaged energy density u_m associated with MO coupling is given by $u_m = (1/4) \text{Re} \mathcal{U}_m$, where

$$\mathcal{U}_m = \begin{pmatrix} E_{\text{S}+}^* & E_{\text{S}-}^* \end{pmatrix} \epsilon_m \begin{pmatrix} E_{\text{I}+} \\ E_{\text{I}-} \end{pmatrix}, \quad (1)$$

and where $\epsilon_m = \epsilon_{m0} + \epsilon_{m+}m_{+'} + \epsilon_{m-}m_{-}$ is a transverse permittivity tensor. The static part ϵ_{m0} is given by Eq. (A2) of appendix A. The diagonal elements of ϵ_{m0} give rise to the static Faraday effect, whereas the static Voigt (Cotton-Mouton) effect originates from the off-diagonal elements of ϵ_{m0} [see Eq. (A2)]. The terms $\epsilon_{m+}m_{+}$ and $\epsilon_{m-}m_{-}$ account for the effect of magnetization precession, where $\epsilon_{m\pm}$ is given by Eq. (A3) of appendix A, and m_{\pm} represent amplitudes of magnetization precession. Note that the matrix $\epsilon_{m\pm}$ is proportional to $e^{\pm i\varphi}$, where φ is the azimuthal angle [see Eq. (A3)]. The spherical symmetry of the FSR is partially broken by the two CFs that are employed for holding it (see Fig. 1).

In the semiclassical approximation V_{SB} is derived from $u_m = (1/4) \text{Re} \mathcal{U}_m$ [see Eq. (1)]. Consider a pair of optical modes having normalized scalar spatial waveforms, which in spherical coordinates are expressed as $u_{n'}(r, \theta, \varphi)$ and $u_{n''}(r, \theta, \varphi)$, respectively. The contribution of this pair to the total interaction term V_{SB} , which is denoted by $V_{n',n''}$, is expressed as

$$V_{n',n''} = a_{n'}^\dagger a_{n''} (g_{n',n'',+} b^\dagger + g_{n',n'',-} b) + \text{h.c.}, \quad (2)$$

where a_n (b) is an annihilation operator for the n 'th optical mode (magnon mode), and h.c. stands for Hermitian conjugate. The coupling coefficients $g_{n',n'',\pm}$ are given by (recall that in our experiment the static magnetic field is normal to the light propagation direction)

$$\hbar^{-1} g_{n',n'',\pm} \simeq g_0 \int d\mathbf{r}' e^{\pm i\varphi} u_{n'}(\mathbf{r}') u_{n''}^*(\mathbf{r}'), \quad (3)$$

where $g_0 = \omega_L Q_s / (8n_0^2 N_s^{1/2})$, and N_s is the number of FSR spins ($N_s = 3.4 \times 10^{16}$ for the FSR under study). For YIG in the telecom band (free space wavelength $\lambda_0 \simeq 1550$ nm), the refractive index is $n_0 = 2.19$, and the dimensionless MO coupling coefficient is $Q_s \simeq 10^{-4}$.

[33], and thus $g_0/(2\pi) = 2.7$ Hz. The overlap integral in Eq. (3) represents a photon-magnon scattering selection rule [11, 12].

The ratio of side band output optical power to the input optical power is denoted by η_{SB} . The largest value of η_{SB} is obtained at the triple resonance [11], for which the MW driving is tuned to the FSR resonance ω_m , the laser frequency ω_L matches the frequency of one optical mode, and the second one has a frequency detuned from ω_L by ω_m . For this case $\eta_{\text{SB}} \simeq (2n_0 R_s g_0/c)^2 N_m$ [it is assumed that the overlap integral in Eq. (3) is of order unity], where N_m is the averaged number of excited magnons in steady state. For the case where the MWA is nearly critically coupled to the FSR, at resonance $N_m \simeq P_p/(\hbar\omega_m\kappa_m)$, where κ_m is the FSR damping rate. The values of $P_p = 20$ dBm, $\omega_m/(2\pi) = 3.8$ GHz and $\kappa_m/(2\pi) = 1$ MHz yield $\eta_{\text{SB}} \simeq 10^{-5}$. This rough estimate agrees with the experimentally observed value of η_{SB} [see Fig. 5].

V. KERR NONLINEARITY

Magnetic anisotropy gives rise to Kerr nonlinearity in the FSR response [34]. The nonlinearity can be exploited for modulation amplification [35]. Modulation measurements in the nonlinear regime are shown in Fig. 6. The results indicate that the Kerr coefficient is negative (giving rise to softening). For the plots shown in the top (bottom) row of Fig. 6, the microwave driving frequency is swept upwards (downwards). The dependency on sweeping direction is attributed to nonlinearity-induced bistability, which, in turn, gives rise to hysteresis.

VI. SUMMARY

In summary, polarization-selective SSM in the telecom band is achieved using an FSR strongly coupled to an LGR. The modulator can be used in a wide optical band, and it is compatible with ultra low temperatures. Future study will explore potential applications, including quantum state readout of superconducting circuits.

This work was supported by the Israeli science foundation, the Israeli ministry of science, and by the Technion security research foundation.

Appendix A: Transverse permittivity tensor

The evolution of electromagnetic waves propagating inside a magnetized medium is governed by a 3×3 permittivity tensor [36–38]. Consider a Cartesian coordinate system (x, y, z) , for which the propagation direction is parallel to the z direction. In this system the static magnetic field (magnetization vector) is parallel to a unit vector denoted by $\hat{\mathbf{h}}$ ($\hat{\mathbf{m}}$). The angle

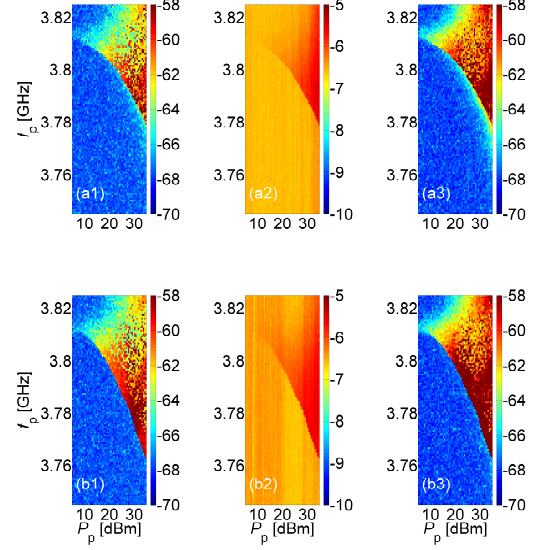


Figure 6: Spectral peaks (in dBm units) in the nonlinear regime as a function of MW driving power P_p . The intensity of the left (right) sideband at wavelength $\lambda_L - \lambda_{\text{SB}}$ ($\lambda_L + \lambda_{\text{SB}}$) is shown in the plots in the left (right) column, whereas the plots in the central column show the intensity of the central optical peak (at TL1 wavelength λ_L). For the plots shown in the top (bottom) row, the frequency f_p is swept upwards (downwards).

between $\hat{\mathbf{h}} = (h_x, h_y, h_z) = (\sin \theta \cos \varphi, \sin \theta \sin \varphi, \cos \theta)$ and $\hat{\mathbf{m}} = (m_x, m_y, m_z)$ is assumed to be small.

From the 3×3 permittivity tensor, a 2×2 transverse permittivity tensor ϵ_T can be derived. In a basis of circular SOP ϵ_T is given by $\epsilon_T = n_0^2 I + \epsilon_m$, where n_0 is the medium refractive index, I is the 2×2 identity matrix, and the 2×2 matrix ϵ_m (in a basis of circular SOPs) is given by [39]

$$\frac{\epsilon_m}{n_0^2} = \begin{pmatrix} Q_s m_z & Q_s^2 m_-^2 \\ Q_s^2 m_+^2 & -Q_s m_z \end{pmatrix}, \quad (\text{A1})$$

where $m_{\pm} = (m_x \pm im_y)/\sqrt{2}$. For YIG in the telecom band, the refractive index is $n_0 = 2.19$, and the dimensionless MO coupling coefficient is $Q_s \simeq 10^{-4}$ [33].

The eigenvalues of ϵ_m/n_0^2 (A1) are given by $\pm Q_s \sqrt{m_z^2 + Q_s^2 m_-^2 m_+^2}$. For the Faraday configuration, for which $m_x = m_y = 0$ and $m_z = 1$, i.e. $\hat{\mathbf{m}}$ is parallel to the propagation direction, the eigenvectors of ϵ_m/n_0^2 represent circular SOPs, the corresponding eigenvalues are $\pm Q_s$, and MO coupling gives rise to circular birefringence, whereas for the Voigt (Cotton-Mouton) configuration, for which $m_z = 0$ and $m_x^2 + m_y^2 = 1$, i.e. $\hat{\mathbf{m}}$ is perpendicular to the propagation direction, the eigenvectors of ϵ_m/n_0^2 represent colinear SOPs, the corresponding eigenvalues are $\pm Q_s^2/2$ [note that $m_-^2 m_+^2 = (m_x^2 + m_y^2)^2/4$], and MO coupling gives rise to colinear

birefringence. Note that for the Faraday configuration, the SOP rotation angle that is accumulated over a traveling distance of a single optical wavelength is $2\pi Q_s$.

To describe the effect of magnetization precession on ϵ_m , it is convenient to express $\hat{\mathbf{m}}$ (magnetization unit vector) as a sum of parallel and perpendicular components, with respect to $\hat{\mathbf{h}}$ (magnetic field unit vector). In a Cartesian coordinate system (x', y', z') , for which the static magnetic field is parallel to the z' direction, the unit vector parallel to the magnetization vector is expressed as $\hat{\mathbf{m}}' = m_{x'}\hat{\mathbf{x}}' + m_{y'}\hat{\mathbf{y}}' + m_{z'}\hat{\mathbf{z}}' = m_+\hat{\mathbf{u}}'_+ + m_-\hat{\mathbf{u}}'_- + m_{z'}\hat{\mathbf{z}}'$, where $\hat{\mathbf{u}}'_\pm = (\hat{\mathbf{x}}' \pm i\hat{\mathbf{y}}')/\sqrt{2}$, and where $m_{\pm'} = (m_{x'} \mp im_{y'})/\sqrt{2}$. The unit vectors $\hat{\mathbf{m}}$ and $\hat{\mathbf{m}}'$ are related by $\hat{\mathbf{m}} = R_{\hat{\mathbf{h}}}^{-1}\hat{\mathbf{m}}'$, where for a given unit vector $\hat{\mathbf{n}}$, the rotation matrix $R_{\hat{\mathbf{n}}}$ is defined by the relation $R_{\hat{\mathbf{n}}}\hat{\mathbf{n}} = \hat{\mathbf{z}}$, and thus $\hat{\mathbf{m}} = m_+\hat{\mathbf{v}}_+ + m_-\hat{\mathbf{v}}_- + m_{z'}R_{\hat{\mathbf{h}}}^{-1}\hat{\mathbf{z}}'$, where $\hat{\mathbf{v}}_\pm = R_{\hat{\mathbf{h}}}^{-1}\hat{\mathbf{u}}'_\pm$. The matrix elements of the 3×3 rotation matrix $R_{\hat{\mathbf{h}}}$ are given by $R_{11} = 1 + (\cos\theta - 1)\cos^2\varphi$, $R_{22} = 1 + (\cos\theta - 1)\sin^2\varphi$, $R_{12} = R_{21} = (1/2)(\cos\theta - 1)\sin(2\varphi)$, $R_{31} = -R_{13} = \sin\theta\cos\varphi$, $R_{32} = -R_{23} = \sin\theta\sin\varphi$ and $R_{33} = \cos\theta$. The following holds $\hat{\mathbf{v}}_\pm =$

$\cos^2(\theta/2)\hat{\mathbf{u}}_\pm - e^{\pm 2i\varphi}\sin^2(\theta/2)\hat{\mathbf{u}}_\mp - 2^{-1/2}e^{\pm i\varphi}(\sin\theta)\hat{\mathbf{z}}$, hence $\hat{\mathbf{m}} = \mu_+\hat{\mathbf{u}}_+ + \mu_-\hat{\mathbf{u}}_- + \mu_z\hat{\mathbf{z}} + m_{z'}\hat{\mathbf{h}}$, where $\mu_\pm = m_{\pm'}\cos^2(\theta/2) - m_{\mp'}e^{\mp 2i\varphi}\sin^2(\theta/2)$ and $\mu_z = -2^{-1/2}(m_+e^{i\varphi} + m_-e^{-i\varphi})\sin\theta$, and thus $m_\pm = \mu_\mp + 2^{-1/2}m_{z'}e^{\mp i\varphi}\sin\theta$.

The assumption that the angle between the static magnetic field and the magnetization vector is small implies that $m_{z'} \simeq 1$ and $|m_{\pm'}| \ll 1$. To first order in $|m_{\pm'}|$, ϵ_m can be expanded as $\epsilon_m = \epsilon_{m0} + \epsilon_{m+}m_+ + \epsilon_{m-}m_-$, where ϵ_{m0} , which is given by [compare with Eq. (A1)]

$$\frac{\epsilon_{m0}}{n_0^2} = \begin{pmatrix} Q_s \cos\theta & \frac{Q_s^2 e^{2i\varphi} \sin^2\theta}{2} \\ \frac{Q_s^2 e^{-2i\varphi} \sin^2\theta}{2} & -Q_s \cos\theta \end{pmatrix}, \quad (\text{A2})$$

accounts for static magnetization, and where $\epsilon_{m\pm}$, which is given by

$$\frac{\epsilon_{m\pm}}{n_0^2} = \frac{Q_s e^{\pm i\varphi} \sin\theta}{\sqrt{2}} \begin{pmatrix} -1 & \pm Q_s(1 \pm \cos\theta) \\ \mp Q_s(1 \mp \cos\theta) & 1 \end{pmatrix}, \quad (\text{A3})$$

accounts for magnetization precession.

-
- [1] Victor Lazzarini, Joseph Timoney, and Thomas Lysaght, “Asymmetric-spectra methods for adaptive fm synthesis”, 2008.
- [2] Wei Li, Wen Ting Wang, Li Xian Wang, and Ning Hua Zhu, “Optical vector network analyzer based on single-sideband modulation and segmental measurement”, *IEEE Photonics Journal*, vol. 6, no. 2, pp. 1–8, 2014.
- [3] S Shimotsu, S Oikawa, T Saitou, N Mitsugi, K Kubodera, T Kawanishi, and M Izutsu, “Single side-band modulation performance of a linbo 3 integrated modulator consisting of four-phase modulator waveguides”, *IEEE Photonics Technology Letters*, vol. 13, no. 4, pp. 364–366, 2001.
- [4] Babak Zare Rameshti, Silvia Viola Kusminskiy, James A Haigh, Koji Usami, Dany Lachance-Quirion, Yasunobu Nakamura, Can-Ming Hu, Hong X Tang, Gerrit EW Bauer, and Yaroslav M Blanter, “Cavity magnonics”, *Physics Reports*, vol. 979, pp. 1–61, 2022.
- [5] Silvia Viola Kusminskiy, “Cavity optomagnonics”, in *Optomagnonic Structures: Novel Architectures for Simultaneous Control of Light and Spin Waves*, pp. 299–353. World Scientific, 2021.
- [6] Na Zhu, Xufeng Zhang, Xu Han, Chang-Ling Zou, and Hong X Tang, “Inverse faraday effect in an optomagnonic waveguide”, *arXiv:2012.11119*, 2020.
- [7] Dominik M Juraschek, Derek S Wang, and Prineha Narang, “Sum-frequency excitation of coherent magnons”, *Physical Review B*, vol. 103, no. 9, pp. 094407, 2021.
- [8] VASV Bittencourt, I Liberal, and S Viola Kusminskiy, “Light propagation and magnon-photon coupling in optically dispersive magnetic media”, *Physical Review B*, vol. 105, no. 1, pp. 014409, 2022.
- [9] Xufeng Zhang, Na Zhu, Chang-Ling Zou, and Hong X Tang, “Optomagnonic whispering gallery microresonators”, *Physical review letters*, vol. 117, no. 12, pp. 123605, 2016.
- [10] Daniel D Stancil and Anil Prabhakar, *Spin waves*, Springer, 2009.
- [11] JA Haigh, Andreas Nunnenkamp, AJ Ramsay, and AJ Ferguson, “Triple-resonant brillouin light scattering in magneto-optical cavities”, *Physical review letters*, vol. 117, no. 13, pp. 133602, 2016.
- [12] A Osada, A Gloppe, Y Nakamura, and K Usami, “Orbital angular momentum conservation in brillouin light scattering within a ferromagnetic sphere”, *New Journal of Physics*, vol. 20, no. 10, pp. 103018, 2018.
- [13] A Osada, R Hisatomi, A Noguchi, Y Tabuchi, R Yamazaki, K Usami, M Sadgrove, R Yalla, M Nomura, and Y Nakamura, “Cavity optomagnonics with spin-orbit coupled photons”, *Physical review letters*, vol. 116, no. 22, pp. 223601, 2016.
- [14] Sanchar Sharma, Yaroslav M Blanter, and Gerrit EW Bauer, “Light scattering by magnons in whispering gallery mode cavities”, *Physical Review B*, vol. 96, no. 9, pp. 094412, 2017.
- [15] Evangelos Almpanis, “Dielectric magnetic microparticles as photomagnonic cavities: Enhancing the modulation of near-infrared light by spin waves”, *Physical Review B*, vol. 97, no. 18, pp. 184406, 2018.
- [16] R Zivieri, P Vavassori, L Giovannini, F Nizzoli, Eric E Fullerton, M Grimsditch, and V Metlushko, “Stokes–anti-stokes brillouin intensity asymmetry of spin-wave modes in ferromagnetic films and multilayers”, *Physical Review B*, vol. 65, no. 16, pp. 165406, 2002.
- [17] BERNARD Desormiere and HENRI Le Gall, “Interaction studies of a laser light with spin waves and magnetoelastic waves propagating in a yig bar”, *IEEE Transactions on Magnetics*, vol. 8, no. 3, pp. 379–381, 1972.
- [18] Zeng-Xing Liu, Bao Wang, Hao Xiong, and Ying Wu,

- “Magnon-induced high-order sideband generation”, *Optics Letters*, vol. 43, no. 15, pp. 3698–3701, 2018.
- [19] Cheng-Zhe Chai, Zhen Shen, Yan-Lei Zhang, Hao-Qi Zhao, Guang-Can Guo, Chang-Ling Zou, and Chun-Hua Dong, “Single-sideband microwave-to-optical conversion in high-q ferrimagnetic microspheres”, *Photonics Research*, vol. 10, no. 3, pp. 820–827, 2022.
- [20] Na Zhu, Xufeng Zhang, Xu Han, Chang-Ling Zou, Changchun Zhong, Chiao-Hsuan Wang, Liang Jiang, and Hong X Tang, “Waveguide cavity optomagnonics for microwave-to-optics conversion”, *Optica*, vol. 7, no. 10, pp. 1291–1297, 2020.
- [21] Jie Li, Yi-Pu Wang, Wei-Jiang Wu, Shi-Yao Zhu, and JQ You, “Quantum network with magnonic and mechanical nodes”, *PRX Quantum*, vol. 2, no. 4, pp. 040344, 2021.
- [22] W Wettling, MG Cottam, and JR Sandercock, “The relation between one-magnon light scattering and the complex magneto-optic effects in yig”, *Journal of Physics C: Solid State Physics*, vol. 8, no. 2, pp. 211, 1975.
- [23] Michael G Cottam and David J Lockwood, *Light scattering in magnetic solids*, Wiley New York, 1986.
- [24] Tianyu Liu, Xufeng Zhang, Hong X Tang, and Michael E Flatté, “Optomagnonics in magnetic solids”, *Physical Review B*, vol. 94, no. 6, pp. 060405, 2016.
- [25] JA Haigh, A Nunnenkamp, and AJ Ramsay, “Polarization dependent scattering in cavity optomagnonics”, *Physical Review Letters*, vol. 127, no. 14, pp. 143601, 2021.
- [26] R Hisatomi, A Noguchi, R Yamazaki, Y Nakata, A Gloppe, Y Nakamura, and K Usami, “Helicity-changing brillouin light scattering by magnons in a ferromagnetic crystal”, *Physical Review Letters*, vol. 123, no. 20, pp. 207401, 2019.
- [27] Ryusuke Hisatomi, Alto Osada, Yutaka Tabuchi, Toyofumi Ishikawa, Atsushi Noguchi, Rekishu Yamazaki, Koji Usami, and Yasunobu Nakamura, “Bidirectional conversion between microwave and light via ferromagnetic magnons”, *Physical Review B*, vol. 93, no. 17, pp. 174427, 2016.
- [28] Douglas M Baney, Bogdan Szafraniec, and Ali Motamedi, “Coherent optical spectrum analyzer”, *Ieee Photonics Technology Letters*, vol. 14, no. 3, pp. 355–357, 2002.
- [29] Maxim Goryachev, Warrick G Farr, Daniel L Creedon, Yaohui Fan, Mikhail Kostylev, and Michael E Tobar, “High-cooperativity cavity qed with magnons at microwave frequencies”, *Physical Review Applied*, vol. 2, no. 5, pp. 054002, 2014.
- [30] Dongshan Zhang, Wenjie Song, and Guozhi Chai, “Spin-wave magnon-polaritons in a split-ring resonator/single-crystalline yig system”, *Journal of Physics D: Applied Physics*, vol. 50, no. 20, pp. 205003, 2017.
- [31] Cijy Mathai, Oleg Shtempluck, and Eyal Buks, “Thermal instability in a ferrimagnetic resonator strongly coupled to a loop-gap microwave cavity”, *Phys. Rev. B*, vol. 104, pp. 054428, Aug 2021.
- [32] Banoj Kumar Nayak, Cijy Mathai, Dekel Meirom, Oleg Shtempluck, and Eyal Buks, “Optical interface for a hybrid magnon-photon resonator”, *Applied Physics Letters*, vol. 120, no. 6, pp. 062404, 2022.
- [33] DL Wood and JP Remeika, “Effect of impurities on the optical properties of yttrium iron garnet”, *Journal of Applied Physics*, vol. 38, no. 3, pp. 1038–1045, 1967.
- [34] Yi-Pu Wang, Guo-Qiang Zhang, Dengke Zhang, Xiao-Qing Luo, Wei Xiong, Shuai-Peng Wang, Tie-Fu Li, C-M Hu, and JQ You, “Magnon kerr effect in a strongly coupled cavity-magnon system”, *Physical Review B*, vol. 94, no. 22, pp. 224410, 2016.
- [35] Cijy Mathai, Sergei Masis, Oleg Shtempluck, Shay Hacohen-Gourgy, and Eyal Buks, “Frequency mixing in a ferrimagnetic sphere resonator”, *Euro. Phys. Lett.*, vol. 131, 2020.
- [36] Ml Freiser, “A survey of magnetooptic effects”, *IEEE Transactions on magnetics*, vol. 4, no. 2, pp. 152–161, 1968.
- [37] Allan D Boardman and Ming Xie, “Magneto-optics: a critical review”, *Introduction to Complex Mediums for Optics and Electromagnetics*, vol. 123, pp. 197, 2003.
- [38] Allan D Boardman and Larry Velasco, “Gyroelectric cubic-quintic dissipative solitons”, *IEEE Journal of selected topics in quantum electronics*, vol. 12, no. 3, pp. 388–397, 2006.
- [39] Eyal Buks and Banoj Kumar Nayak, “Quantum measurement with recycled photons”, *Physical Review B*, vol. 105, no. 1, pp. 014421, 2022.